Supporting Information
Hierarchical multivalent effects control influenza host specificity

Nico J. Overeem[1], P. H. (Erik) Hamming[1], Oliver C. Grant[2], Daniele Di Iorio[1], Malte Tieke[3], M. Candelaria Bertolino[1]†, Zeshi Li[4], Gaël Vos[4], Robert P. de Vries[4], Robert J. Woods[2]*, Nicholas B. Tito[5], Geert-Jan P. H. Boons[2,4,6,7]*, Erhard van der Vries[3,8,9]*, Jurriaan Huskens[1]*

[1]Molecular Nanofabrication Group, MESA+ Institute for Nanotechnology, Faculty of Science and Technology, University of Twente, P.O. Box 217, 7500 AE Enschede, The Netherlands; contact: j.huskens@utwente.nl

[2]Complex Carbohydrate Research Center, University of Georgia, 315 Riverbend Rd, Athens, GA 30602, USA; contact: rwoods@ccrc.uga.edu

[3]Division of Virology, Department of Infectious Diseases and Immunology, Faculty of Veterinary Medicine, Utrecht University, 3584 CL Utrecht, The Netherlands.

†INFIQC, Departamento de Química Orgánica, Facultad de Ciencias Químicas. Universidad Nacional de Córdoba, Ciudad Universitaria (X5000HUA), Córdoba, Argentina

[4]Department of Chemical Biology & Drug Discovery, Utrecht Institute for Pharmaceutical Sciences, Utrecht University, 3584 CG Utrecht, The Netherlands; contact: g.j.p.h.boons@uu.nl

[5]Electric Ant Lab, Science Park 106, 1098 XG Amsterdam, The Netherlands.

[6]Bijvoet Center for Biomolecular Research, Utrecht University, Utrecht, the Netherlands.

[7]Department of Chemistry, University of Georgia, Athens, GA 30602, USA.

[8]Royal GD, Arnsbergstraat 7, 7418 EZ, Deventer, The Netherlands; contact: e.vd.vries@gdanimalhealth.com

[9]Department of Clinical Chemistry and Haematology, University Medical Center Utrecht, Utrecht University, Utrecht, The Netherlands.

Supporting Figures

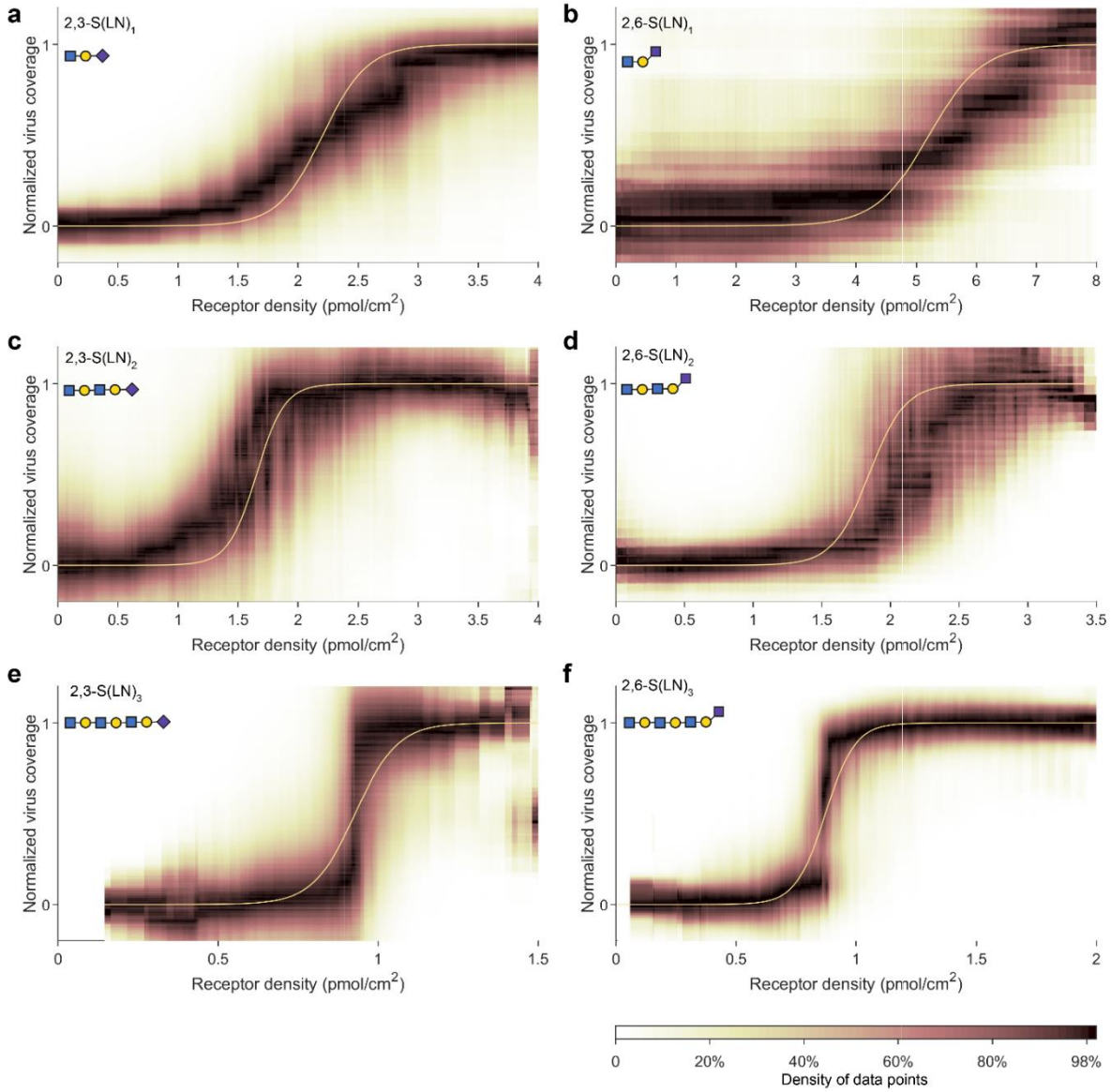

Figure S1. Binding profiles of influenza virus with multivalent affinity profiling. Data points are shown in a density map that was generated with a rolling average of 2001x250 points, a window of 40, and a range of 0.1 in the y-direction unless otherwise specified. The density of data points is normalized for each window, because the density of data points is much higher on the left side of the graphs due to the exponential shape of the receptor gradients. The fitted curves are the same as in Figure 2d. **a,** 2,3-S(LN)$_1$, N=1,530,544 from 6 pairs of micrographs. **b,** 2,6-S(LN)$_1$, N=92,480 from 2 pairs of micrographs, range=0.3. **c,** 2,3-S(LN)$_2$, N=406,912 from 3 pairs of micrographs. **d,** 2,6-S(LN)$_2$, N=203,456 from 3 pairs of micrographs. **e,** 2,3-S(LN)$_3$, N=369,920 from 3 pairs of micrographs. **f,** 2,6-S(LN)$_3$, N=406,912 from 3 pairs of micrographs.

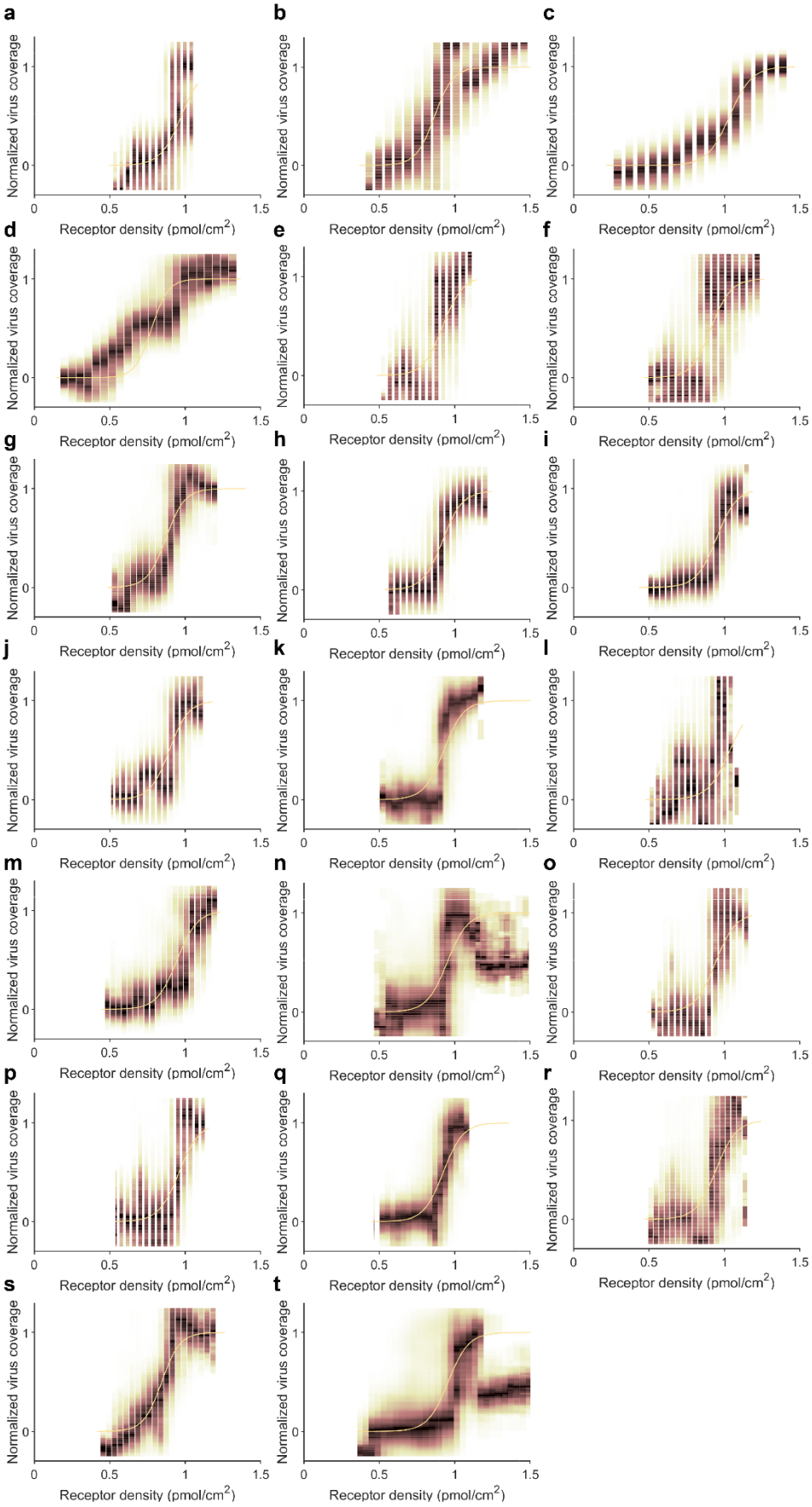

Figure S2. Typical example of multiple binding profiles of PR8 obtained with multivalent affinity profiling. **a-t**, fitted binding profiles in 20 corrals that compose the binding profile of 2,3-S(LN)$_3$ shown in Figure S1e.

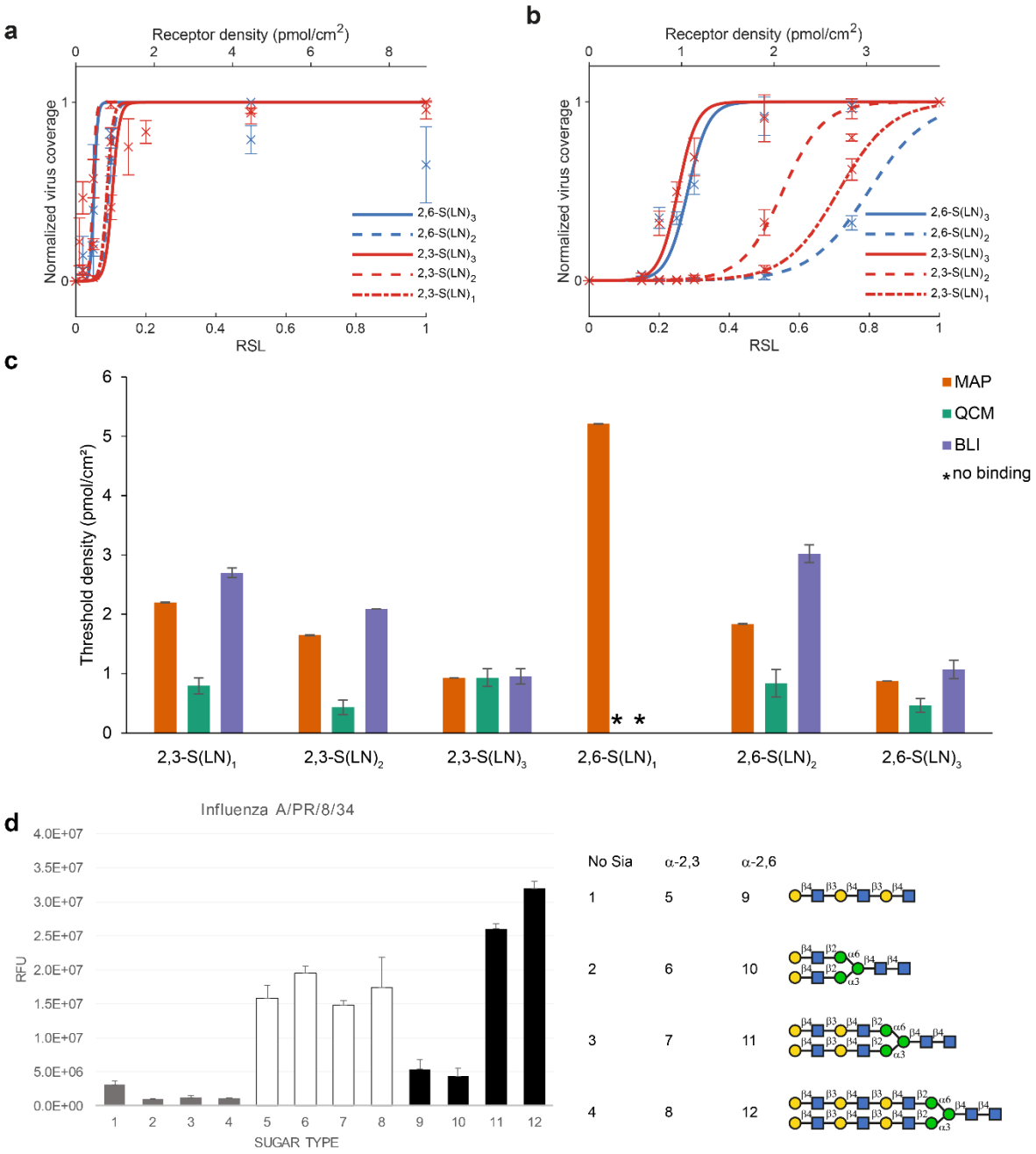

Figure S3. Binding profiles of influenza virus on different platforms. a, Binding profiles as function of receptor density in QCM. **b,** Binding profiles as function of receptor density in BLI. **c,** Overview of threshold receptor densities for MAP, QCM, and BLI. **d,** Fluorescence intensities of PR8 binding on a glycan array. Binding to a linear 2,6-S(LN)$_3$ (#9) and to a branched 2,6-S(LN)$_1$ glycan (#10) are both much lower than either their 2,3-linked counterparts (#5 and 6) or branched 2,6-S(LN)$_2$ and 2,6-S(LN)$_3$ (#11 and 12), suggesting that PR8 is also more sensitive to the branching of 2,6- than of 2,3-linked glycans.

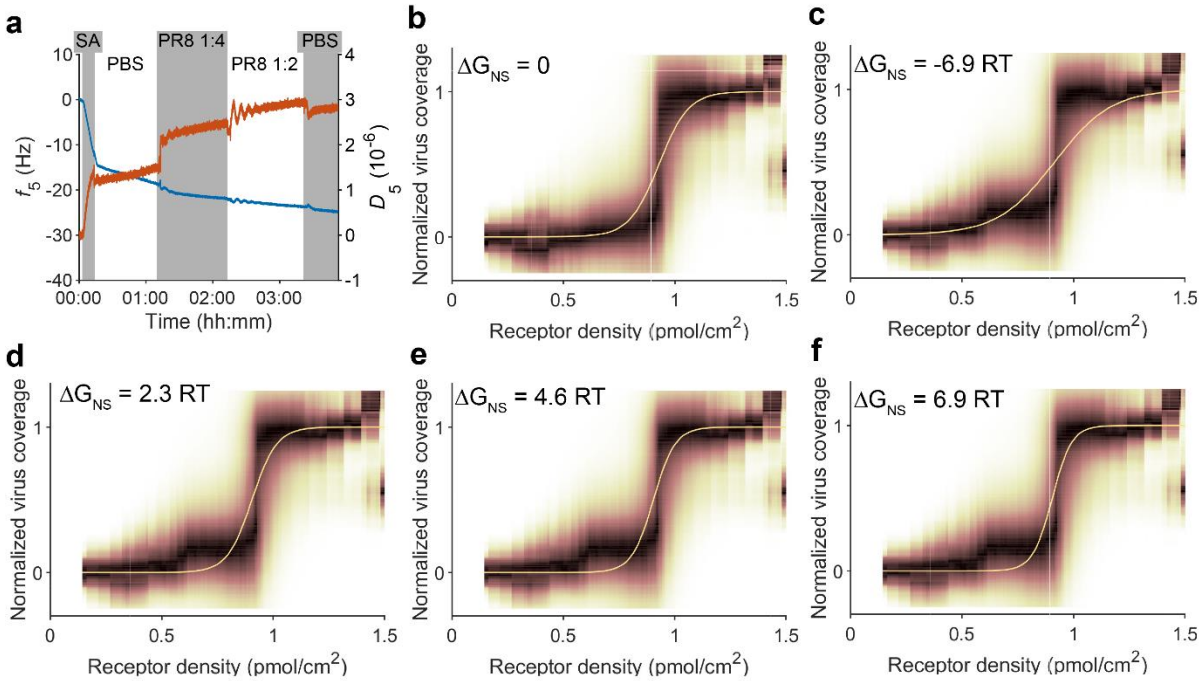

Figure S4. Role of nonspecific binding in PR8 binding and data fitting. a) Frequency and dissipation shifts in QCM-D. As a negative control, an SLB of MPPC was functionalized with SA but not with glycans. PR8 was passed over the SLB at concentrations of $2.5 \cdot 10^9$ vp/ml and $5 \cdot 10^9$ vp/ml, with 100 µM Zanamivir. The 5th overtone is shown. The virus binding to the SA-modified SLB is negligible. **b)** Binding profile of PR8 on 2,3-S(LN)$_3$ fitted with Equation S6 using $\Delta G_{NS} = 0$, so that it simplifies to Equation 1. Profile and fit are the same as in Figure S1e. **c)** The same binding profile fitted with $\Delta G_{NS} = -6.9$ RT. **d)** The same binding profile fitted with $\Delta G_{NS} = 2.3$ RT. **e)** The same binding profile fitted with $\Delta G_{NS} = 4.6$ RT. **f)** The same binding profile fitted with $\Delta G_{NS} = 6.9$ RT.

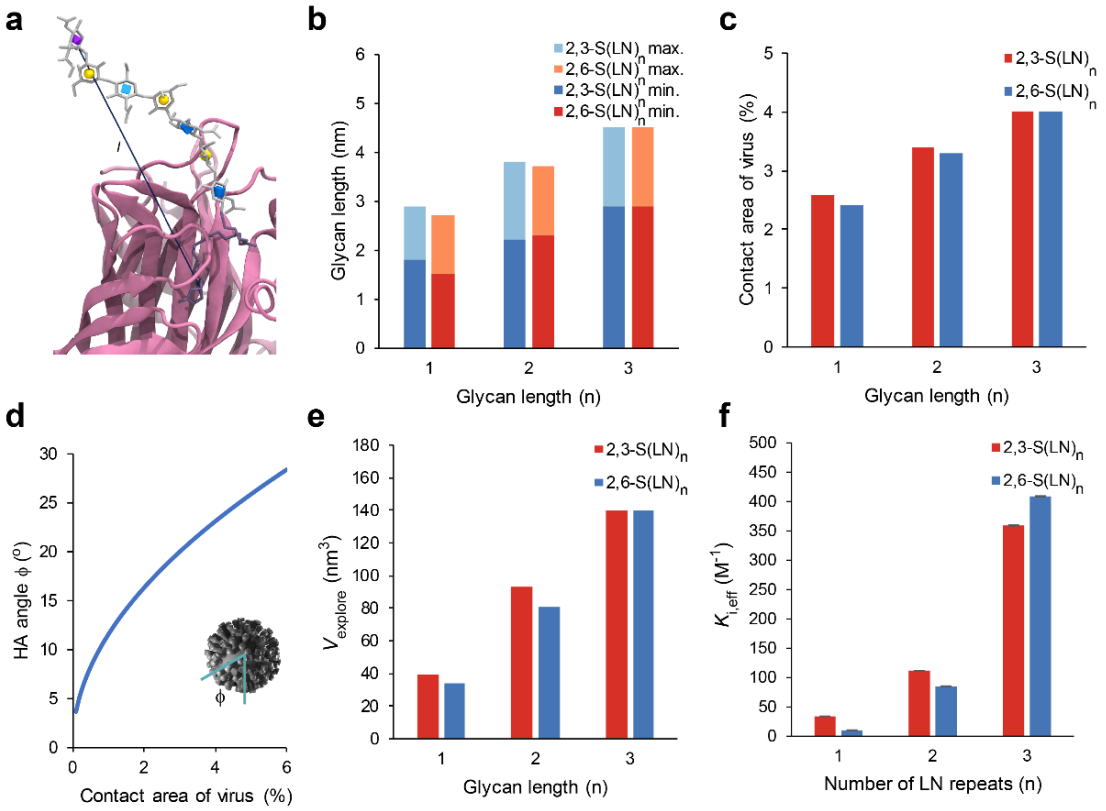

Figure S5. Estimation of the virus contact area of PR8 and explored volume of receptors from glycan length to determine the effective monovalent equilibrium constants of the HA-glycan interactions. a, Molecular dynamics snapshot showing how the distance between biotin and sialic acid was determined. **b**, Minimum and maximum distances between biotin and sialic acid for different glycan types as determined with MD. **c**, Contact area of PR8 corresponding to the maximum length of the different glycans. Longer glycans can reach RBDs that are farther away from the surface. **d**, The maximum angle of HA with respect to the surface as function of contact area. 0° is perpendicular to the surface. If SA can titlt 16° with respect to the surface, the maximum angle between HA and SA is 34-39°, which is less than the optimal angle (Figure 4b), suggesting that the RBDs close to the edge of the contact area contribute most strongly to the average $K_{i,eff}$. It is therefore reasonable to assume the maximum value for $A_{contact}$. **e**, Values for $V_{explore}$ based on the volume between two half-spheres with the minimum and maximum glycan length as radius. **f**, Values for $K_{i,eff}$ calculated from $V_{explore}$ and the fitted values for $K_{i,eff}/(N_A V_{explore})$.

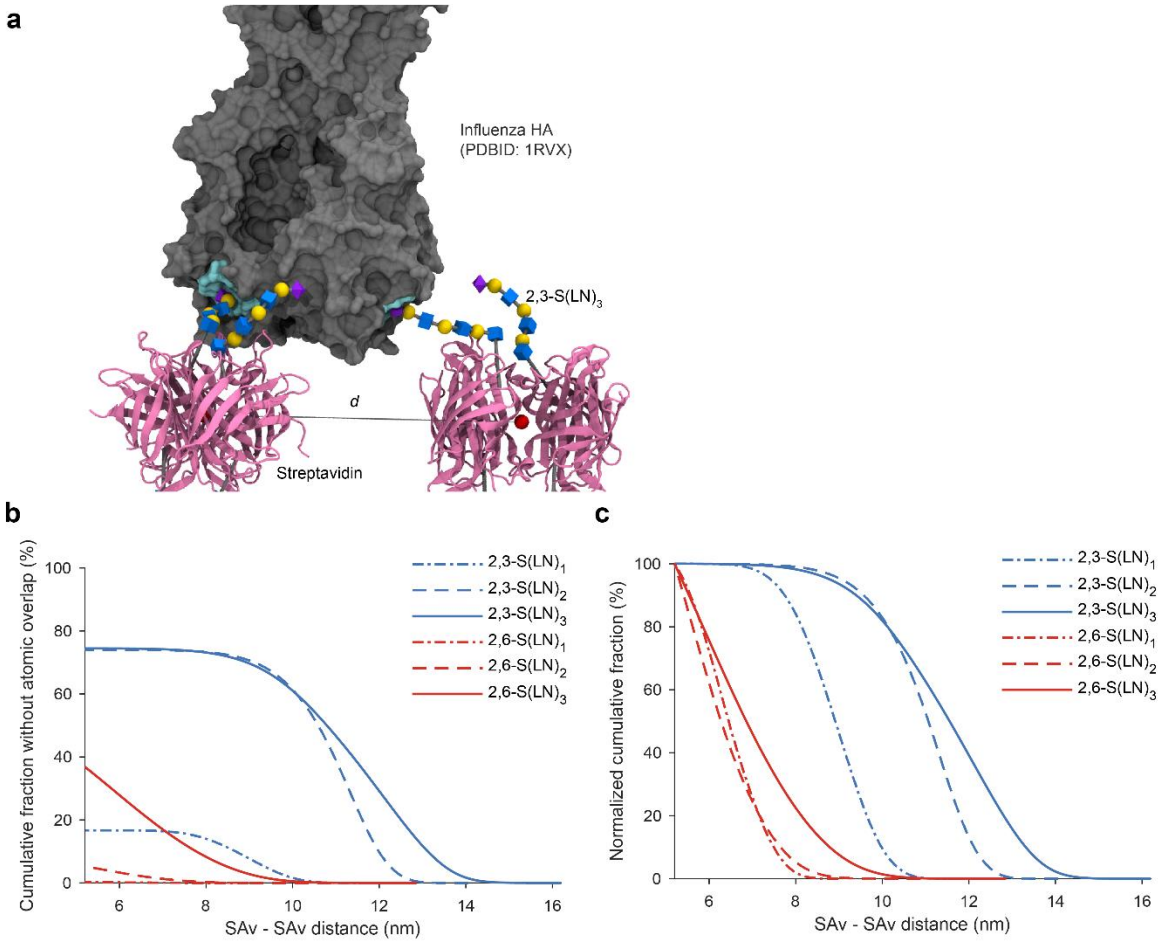

Figure S6. The availability of the 1 HA – 2 SA mode depends on the receptor type and the distance between the SAs. a, Illustration of the 1 HA – 2 SA multivalent binding mode. The biotinylated glycan from two SA proteins (pink ribbon) are aligned into two independent binding sites of an influenza HA. The availability of this binding mode is directly related to density of SA on the surface and the shapes adopted by each glycan. **b,** Cumulative fraction of glycan shapes for which glycans on different SA proteins can bind to the same HA trimer without atomic overlap as function of the distance between the two SAs. The fraction is shown as percentage of all possible shapes. **c**, The cumulative fraction of glycan shapes from Figure S6b is normalized to show the differences in how the availability of this mode depends on the SA-SA distance for each glycan type.

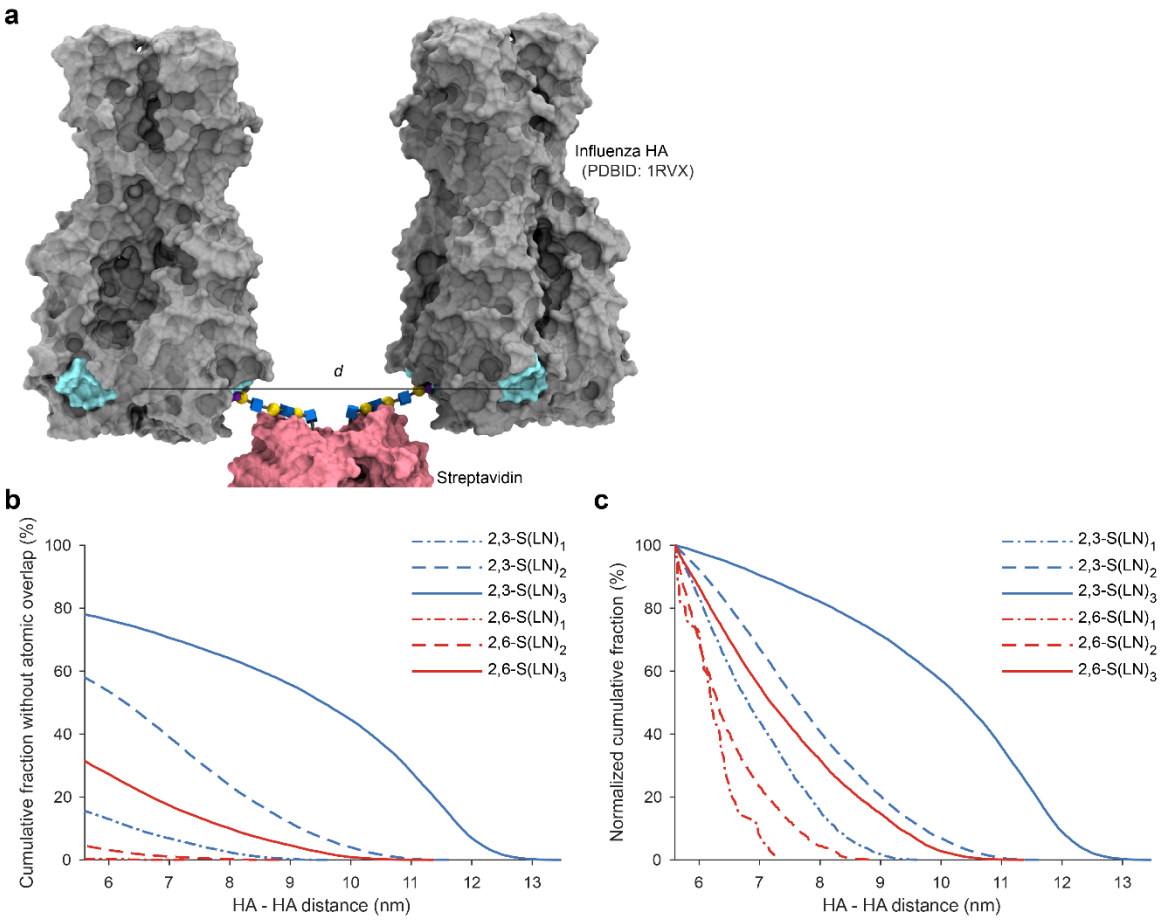

Figure S7. The availability of the 2 HA – 1 SA mode depends on the receptor type and the distance between the SAs. a, Illustration of the 2 HA – 1 SA multivalent binding mode. The biotinylated glycans from one SA protein (pink) are aligned into two binding sites on different HA trimers. The availability of this binding mode is directly related to density of HA on the virus and the shapes adopted by each glycan. **b,** Cumulative fraction of glycan shapes for which glycans on one SA proteins can bind to different HA trimers without atomic overlap as function of the distance between two the HAs. For 2,6-S(LN)$_1$ this mode is hardly available even between close-packed HAs. **c**, The cumulative fraction of glycan shapes from Figure S7b is normalized to show the differences in how the availability of this mode depends on the HA-HA distance for each glycan type.

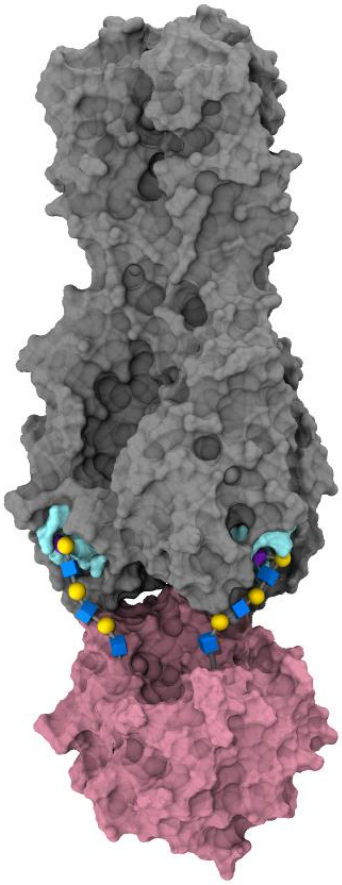

Figure S8. 3D model of bidendate binding between 2,6-S(LN)$_3$-SA and HA (PDB ID: 3UBE). The model was generated by superimposing to the Sia-Gal motif in the crystal structure and using a previously reported protocol to bring the second glycan into the second binding site of HA. The bidendate mode was stable throughout an unrestrained 100 ns MD simulation.

Supporting Discussion 1

Derivation and fitting of theoretical binding model

We derive an expression for the equilibrium binding constant ("avidity constant") of a ligand-coated virus particle binding to a receptor-coated surface. The expression is converted into a form that can be readily used by inputting experimental parameters, and applied to generate a Langmuir adsorption isotherm for virus binding (as a function of solution concentration and substrate receptor density).

Avidity constant

Consider viruses with a diameter of *d*. When the virus is adjacent to the receptor surface, then a fraction of the virus's outer shell is in contact with the surface. The contact area A_{contact} is defined as the receptor surface area over which RBD-glycan pairs can be formed to a single virus particle. Furthermore, let σ_L be the number of ligands per unit area on the virus exterior, and σ_R be the number of receptors per unit area on the receptor surface. The receptors are assumed to be Poisson distributed and/or mobile on the receptor surface. The HA ligands on the virus surface are assumed to be uniformly distributed, and they are are embedded in a rather densely packed corona. As a result, a given RBD has limited configurational flexibility, and may only bind to the nearest glycan on the adjacent receptor surface.

Reference [1] outlines the statistical thermodynamics of multivalent binding in the regime where ligands and receptors are short and with limited configurational flexibility, so that each may only bind to the nearest partners within a given microscopic range. Drawing from their derivations as a starting point, we define the binding partition function for our present scenario of virus binding as follows:

$$Q_{bind} = \left(1 + e^{-\Delta G_{lig}/RT}\right)^{\tilde{N}} e^{-\Delta G_{NS}/RT} e^{\mu^{\circ}/RT} \qquad \text{(S1)}$$

where

- $\tilde{N} = A_{\mathrm{contact}} \cdot \min(\sigma_R, \sigma_L)$ is the average total number of possible simultaneous bonds that may be formed between a bound virus particle and the receptor surface;
- ΔG_{lig} is the free energy for making a single ligand-receptor (here: RBD-glycan) bond;
- R is the ideal gas constant;
- T is the temperature;
- ΔG_{NS} is any overall non-specific virus-surface interaction free energy
- μ° is the chemical potential of the viruses in solution at standard 1 molar concentration.

Inclusion of the chemical potential weight in Q_{bind} accounts for the thermodynamic cost of drawing in a virus particle from the bulk solution in order to bind it to the receptor surface.

We now translate Equation S1 into the avidity constant K_{av}. First, the total ligand-receptor binding free energy ΔG_{lig} contains several contributions:

$$\Delta G_{lig} = -RT \ln\left(\frac{K_i^{\circ}}{N_A h_{bind} A_{reach}}\right) + \Delta G_{lig,cnf} \qquad \text{(S2)}$$

The first term contains the contribution from K_i°, the ligand-receptor binding equilibrium constant in free solution. The quantity V_{explore} is the local volume of space that the RBD and glycan binding units may explore, given that they are tethered to the virus and sensor substrate,

respectively. Thus, the quantity $1/N_A V_{explore}$ is the "effective molarity" of glycan on the surface, from the perspective of a single RBD on a bound virus. The second term $\Delta G_{lig,cnf}$ accounts for any additional free energy cost for making a ligand-receptor bond, e.g. if the ligand or receptor experience any further restriction on their internal degrees of freedom, or if there are additional ligand-receptor steric interactions.

Next, the chemical potential μ is related to the molar concentration $[V]$ of virus in solution by

$$\frac{\mu}{RT} = \ln(N_A V_{ex}[V]) + \text{excess chemical potential terms,} \quad \text{(S3)}$$

where V_{ex} is the occupied volume of a virus particle usually taken to be d^3 or $\frac{4\pi}{3}(d/2)^3$. The standard chemical potential in Equation S1 is simply Equation S3 evaluated at the standard concentration of $[V]$ = 1 M (one molar), assuming ideal solution conditions:

$$\frac{\mu^\circ}{RT} = \ln(N_A V_{ex}\,[1\,M]) \quad \text{(S4)}$$

Lastly, we assume that the viruses pack on the surface at a maximum possible packing fraction of ϕ (a value between zero and one). The amount of surface area excluded by a virus when it is bound to the surface is A_{ex}.

The equilibrium avidity constant K_{av} is obtained from Q_{bind} by the thermodynamic relations

$$\Delta G^\circ_{bind} = -RT \ln Q_{bind} = -RT \ln([1\,M]\,K_{av}) \quad \text{(S5)}$$

With this, Equation S1, and the previous substitutions, we arrive at:

$$K_{av} = N_A V_{ex} e^{-\Delta G_{NS}/RT}\left(1 + \frac{K_i}{N_A V_{explore}} e^{-\Delta G_{lig,cnf}/RT}\right)^{\tilde{N}} \quad \text{(S6)}$$

This expression yields K_{av} in units of inverse molarity (dm³/mol) by expressing length-derived quantities in dm, and K_i in M^{-1}. The free energy quantities can be expressed in any energy units compatible with those chosen for RT.

Virus adsorption isotherm

We now derive the adsorption profile (isotherm) for virus binding on a receptor-coated substrate surface, given that the substrate has a density σ_R of receptors, and the viruses are at a bulk solution (or flow) concentration of $[V]^\circ$.

The avidity constant is related to the equilibrium concentrations of free and bound multivalent viruses in a solution via:

$$K_{av} = \frac{[R]_{occupied}}{[V]_{free}[R]_{free}}. \quad \text{(S7)}$$

Here, $[R]_{occupied}$ is the concentration of receptors "occupied" on the substrate: either bound to or sterically blocked by a substrate-bound virus particle. The quantity $[V]_{free}$ is the concentration of viruses that are not bound (i.e. free in solution), and $[R]_{free}$ is the concentration of substrate receptors that are available for binding—e.g. neither bound to a ligand, nor sterically blocked by a nearby bound virus.

The first step we take is to assume that the *number* of viruses in solution far exceeds the number that can possibly bind to the substrate. This condition can be met if, for example, the volume

of our "virus solution" is very large compared to the size of the substrate that the viruses can bind to, or if the substrate is being exposed to a continuous flow of a virus solution at a fixed concentration. In these cases, the solution concentration of unbound viruses is assumed to be a constant with respect to how many bind to the substrate. Therefore, the previous equation simplifies to

$$K_{av} = \frac{[R]_{occupied}}{[V]^{\circ}[R]_{free}}, \tag{S8}$$

where $[V]^{\circ}$ is the input bulk solution concentration of viruses.

When a virus binds to the substrate, it blocks all receptors that are directly below it over an area of A_{ex}. Thus, the concentration of occupied receptors $[R]_{occupied}$ in the system is just the number N_{bound} of bound viruses times the average number of receptors they each occupy, $A_{ex}\sigma_R$, divided by the volume V_{sys} of the sample:

$$[R]_{occupied} = \frac{N_{bound}A_{ex}\sigma_R}{V_{sys}\phi}, \tag{S9}$$

where σ_R is the number of receptors per unit area on the substrate. Dividing by ϕ here incorporates the packing efficiency of the binding viruses. Similarly, the concentration $[R]_{free}$ of free receptors is the concentration of all receptors $[R] = A_{sfc}\sigma_R/V_{sys}$ (where A_{sfc} is the total area of the substrate) minus the concentration $[R]_{occupied}$ that is occupied:

$$[R]_{free} = \frac{1}{V_{sys}}\left(A_{sfc}\sigma_R - \frac{N_{bound}A_{ex}\sigma_R}{\phi}\right), \tag{S10}$$

Inserting these definitions into Equation S8 yields

$$K_{av} = \frac{1}{[V]^{\circ}}\left[\frac{\frac{1}{\phi}\left(\frac{N_{bound}A_{ex}}{A_{sfc}}\right)}{1-\frac{1}{\phi}\left(\frac{N_{bound}A_{ex}}{A_{sfc}}\right)}\right]. \tag{S11}$$

Defining $\theta = N_{bound}A_{ex}/A_{sfc}$ as the fraction of binding positions occupied by viruses at equilibrium, we arrive at

$$K_{av} = \frac{1}{[V]^{\circ}}\left[\frac{(\theta/\phi)}{1-(\theta/\phi)}\right]. \tag{S12}$$

Solving for θ yields

$$\theta = \phi\left(\frac{K_{av}[V]^{\circ}}{1+K_{av}[V]^{\circ}}\right). \tag{S13}$$

This may be equivalently expressed in number of bound viruses per unit surface area by

$$\rho_{bound} = \frac{\phi}{A_{ex}}\left(\frac{K_{av}[V]^{\circ}}{1+K_{av}[V]^{\circ}}\right). \tag{S14}$$

Application of the theoretical model to experimental data

To determine the number of interactions at the threshold, we applied the theoretical model to the MAP data. Normalized virus coverage is plotted against receptor density for each corral (Figure S2). Binding profiles on multiple corrals, from multiple positions in the microchannel and multiple experiments, are combined into a single binding profile on which the fitting is performed (Figure S1). This afforded a better fit than the average of each corral. The virus

concentration [V] and diameter were characterised with nanoparticle tracking analysis (NTA) and V_{ex} was calculated from the virus diameter. We used [V] = 10^9 particles/ml and d = 112 nm. We found that the threshold receptor density did not change over time (data not shown), so that the profile of normalised virus binding as function of σ_R was the same as the profile of θ and ϕ = 1 could be used.

To test the role of nonspecific binding on the SLBs in the MAP chip, we prepared an SLB of MPPC with 0.5% biotin-cap-DOPE in a SiO_2-coated sensor in QCM-D and modified it with SA but not with glycans (Figure S4a). We passed PR8 over the SLB in concentrations of $2.5 \cdot 10^9$ vp/ml and $5 \cdot 10^9$ vp/ml in the presence of 100 µM Zanamivir. Apart from some baseline drift and noise at solution changes, the shifts in frequency upon passing PR8 over the SLB are negligible and may be attributed to viscosity or refractive index changes as they are rapidly reversed upon changing the solution to PBS.We tested the effect of ΔG_{NS} on the fits by fitting the binding profile of 2,3-S(LN)$_3$ with different values of ΔG_{NS} (Figure S4b – S4f) and found that positive (repulsive) values for ΔG_{NS} lead to steeper binding profiles, whereas negative values lead to less steep profiles. A two-parameter fit with ΔG_{NS} as extra free parameter appeared too sensitive towards noise around the threshold receptor density which led to it fitting strongly negative values for ΔG_{NS} to the steep profiles of S(LN)$_3$. Upon visual inspection of the binding profiles and fits in Figure S1, S(LN)$_3$ appears to have a positive ΔG_{NS}, whearas S(LN)$_1$ may have a negative ΔG_{NS}. Possibly, the longer glycans provide a stronger steric repulsion. This means that no uniform assumption can be made with regards to ΔG_{NS} as it may likely vary with contact area and glycan density as well.

Because we did not observe nonspecific binding, we assume in this study for the sake of simplicity that $\Delta G_{NS} = 0$. Because $\Delta G_{lig,cnf}$, and K_i° could not be fitted independently, we use $K_{i,eff} = K_i^\circ e^{-\Delta G_{lig,cnf}/RT}$ to account for any differences between the K_i° of a free glycan and RBD in solution and the effective K_i at the surface, such as steric repulsion between SA on the surface and HA. This way, Equation S13 simplifies to

$$\theta = \frac{K_{av}[V]^\circ}{1+K_{av}[V]^\circ} \tag{S15}$$

and Equation S6 simplifies to Equation 1.

We used the maximum contact area to fit the profile of θ as function of σ_R with $K_{i,eff}/N_A V_{explore}$ as free parameter. The model in Figure 4c implies that the maximum contact area is bound by the maximum distance at which a glycan can reach an RBD. We used molecular dynamics to determine the minimum and maximum distance between sialic acid in the RBD and biotin in the binding pocket of SA (Figure S5a and S5b). The maximum contact area that can be reached by glycans of this length is shown in Figure S5c.

Due to the curvature of the virus, a larger contact area not only means that RBDs are farther from the surface, but also that the angle between HA and SA is larger (Figure S5d). We hypothesized that glycan-RBD interactions farther away from the surface would be less favorable. Instead we found with molecular dynamics that the most favorable angle between HA and SA is between 30° and 100° and interactions are much less likely when HA and SA are in a straight line (Figure 4b). At virus contact areas of 2.4-4.0%, the angle of HA is 17.8-23.1°. We estimate that SA can tilt approximately 16°, allowing a maximum angle between HA and SA of 34-39°. This suggests that for all glycans in this study, the RBDs close to the

edge of the contact area contribute most strongly to the average $K_{i,eff}$. We estimate that $V_{explore}$ is the volume between a half-sphere with the minimum glycan length as radius and one with the maximum as radius (Figure S5e). Using the fitted values for $K_{i,eff}/N_A V_{explore}$, we calculate the average $K_{i,eff}$ for each glycan type (Figure S5f).

Supporting Discussion 2

Modes of HA-glycan complexation

Molecular modelling of HA-glycan binding

MD simulations were employed to explore the possible shapes that the S(LN)$_n$ glycan-linker-biotin molecule can adopt when it is bound to the SA tetramer, thus to understand the influence of glycan length, structure and presentation on the virus binding. The percentage of shapes for each SA-immobilized glycan type that could allow HA binding were determined (Figure 4b). In general, as the glycan becomes shorter, it displays fewer shapes compatible with HA binding, particularly in the case of 2,6-S(LN)$_1$, which correlates with the observed avidity data (Figure 2e). The decrease in shapes compatible with HA binding corresponds to the decrease in conformational entropy of the glycans, but ignores interactions between the HA head and LN repeats.[2]

To take into account the orientational constraints of the HA and SA molecules that arise from their immobilization on the virus and array surfaces, respectively, the angle between the centre lines of the HA and SA were determined (illustrated in Figure 4a). Based on a simple geometric model (Figure 4c) for a spherical virus interacting with glycans projecting from a flat SA surface, the allowable angular range for the glycan relative to the surface depends on the glycan length and the virion radius. The MD data were used to provide estimates of the average glycan length for each type of glycan bound to SA, and the radius of the virion was measured with nanoparticle tracking analysis. With these values, the allowable angles ranged from 0 to 17.8° for the shortest glycans and up to 23.1° for the longest. Additionally, we estimate that SA may tilt up to 16°, so that HA-SA angles of up to 39° are allowable. Even with the tilting of SA, these ranges represent only a small subset of the orientations that would be allowable were the glycan not immobilized on a flat surface.

For each glycan, the total number of orientations with allowable angles correlates well with the observed dependence on receptor densities (Figure 2); the shorter glycans, especially 2,6-S(LN)$_1$, have fewer acceptable glycan poses, and therefore require a higher receptor density to bind the virus. The longer glycans having a higher number of acceptable orientations can bind the virus at lower glycan densities. Examining the dependence of the acceptable angle range as a function of sialoside linkage type, the theoretical data also indicate that the 2,6-S(LN)$_1$ glycan has markedly fewer acceptable orientations compared to the 2,3-S(LN)$_1$ glycan, consistent with the density dependence in Figure 2.

Multivalent binding mode of 1 HA with multiple SA molecules

The geometry corresponding to a single HA trimer binding to two separate SA-glycan complexes (1 HA – 2 SA) was generated from the MD simulations of each glycan type. The separation distance between the centers of two SA tetramers bound in two separate binding sites of the HA trimer was computed (Figure S6a). Each shape from the MD simulation (n=4000) was compared against all other shapes in the second HA binding site ($7.998 \cdot 10^6$ combinations). Any shape combination that oriented the SAs such that they would overlap (distance < 5.2 nm) were discarded. The cumulative fraction of shapes that were not discarded are reported in Figure S6b as function of the distance between the approaching SAs.

Multivalent binding mode of 2 HA trimers with glycans on a single SA

The ability for each glycan to form the 1SA – 2 HA binding mode (Figure S7a)was assessed by calculating the distance between the HA headgroup center (average value of each Sia C2 atom) and the SA tetramer center line, then doubling the value. Any values that were less than the diameter of a HA headgroup (5.6 nm) were discarded. The cumulative fraction of shapes that were not discarded are reported in Figure S7b as function of the distance between the approaching HAs.

Bidendate binding mode of 1HA – 1SA

The linear inter-binding site distance on an HA trimer is ~45 Å, however, this ignores that any bidendate molecule will have to span over/around the head group and that the binding sites require a particular orientation of the Sia-Gal. Following a previously reported protocol[3], glycans with shapes that are theoretically long enough to span two binding sites on a HA (>45 Å) were checked by superimposing one of the binding motifs into the crystal structure, and then adjusting the intervening glycosidic linkages within known ranges to bring the second binding motif into the second binding site, without causing atomic overlaps between the glycan or the SA and the HA headgroup. Once the second motif is within ~5 Å, restraints are gradually introduced over the course of an MD simulation to pull the Sia-Gal disaccharide in into the binding position observed in the corresponding crystal structure. Bidendate binding is deemed possible for a glycan if it is able span two binding sites and then remain bound during an extended (> 100 ns), unrestrained MD.

The analysis found that only the SA bearing 2,6-S$(LN)_3$ glycans was capable of forming a bidendate interaction with a single HA (Figure S8). The other glycans (2,6-S$(LN)_1$, 2,6-S$(LN)_2$ and all of the 2,3-linked glycans) were either too short or, in the case of 2,3-S$(LN)_3$, the required orientation of both motifs could not be achieved.

Methods

Biotinylated glycan preparation

Glycans were prepared based on already reported procedures.[4,5] Biotinylated LacNAc was synthesized chemically and used as starting material for one-pot enzymatic extension. Briefly, the starting disaccharide was dissolved in 100 mM MOPS buffer pH 7.2 to a 10 mM working concentration. UDP-GlcNAc (20 mM, 2 eq.), $MnCl_2$ (10 mM) and calf-intestine alkaline phosphatase (10 U/ml) were added. The GlcNAc transferase beta3GnT2-GFP was then added at the working concentration of 0.1 mg/ml. The reaction solution was incubated at 37 °C for 24 h under mild agitation. The solution was heated to 100 °C for 10 min to denature the enzymes if no starting material was observed by ESI-MS. Otherwise another 0.05 mg/ml glycosyltransferase was added, and the reaction was incubated for another 24 h. After cooling to room temperature, UDP-Gal (2 eq.) and the galactosyltransferase B4GalT1 was added at the working concentration of 0.1 mg/ml. The solution was incubated overnight at 37 °C to allow galactosylation to go to completion (monitored by ESI-MS). Enzyme denaturization was performed as mentioned for beta3GnT2. This tandem enzymatic treatment (beta3GnT2-B4GalT1) was repeated to afford triLacNAc structure without any intermediate column chromatography-based purification. In between each reaction, the solution was replenished with fresh UDP-sugar donors (1 eq.), $MnCl_2$ and alkaline phosphatase. When the precipitate (generated during beta3GnT2 treatment) became over half of the volume, the mixture was spun down and the supernatant was transferred into a new vial. The precipitate was washed with 1/5 initial reaction volume of buffer, spun down and the supernatant was combined.The solution containing triLacNAc-biotin was freeze-dried and purified with biogel-p2 to give the pure product in ~60% yield.

The triLacNAc-biotin was then sialylated in α2,6-linkage with ST6Gal1 and α2,3 with ST3Gal4. The triLacNac-biotin was dissolved in 100 mM TRIS buffer pH 8 to a 10 mM working concentration. CMP-Neu5Ac (15 mM, 1.5 eq.), bovine serum albumin (0.1 mg/ml), calf-intestine alkaline phosphatase (10 U/ml) and the appropriate sialyltransferase (0.1 mg/ml) were added. The solution was incubated overnight at 37 °C to allow sialylation to go to completion (monitored by ESI-MS).The resulting heptasaccharide was purified with biogel-p2 and fractions containing carbohydrate were pooled and freeze-dried to give the pure form as a white crystalline powder for subsequent experiments.

Virus stock preparation

Influenza A/Puerto Rico/8/34 virus (Mt. Sinai strain) stocks were prepared by propagating the virus in 10-days-old embryonated chicken eggs (GD Animal health, Deventer, the Netherlands) at 33°C. Allantoic fluids were harvested after 48-72 h and cleared from debris by centrifugation at 3,000 rpm for 10 min at 4°C. Subsequently, the viruses were pelleted by centrifugation at 7,000 rpm for 18 h at 4°C and resuspended in PBS (pH 7.4) (Lonza). Viruses were then purified further by loading of the virus sample on a discontinuous sucrose gradient (10-50% w/v) and centrifugation for 45 min at 25,000 rpm using a SW41 swing-out rotor. The virus-containing sucrose layer was finally harvested and dialyzed (Slide-A-Lyzer, Thermo Scientific) for 48 h at 4°C to remove the remaining sucrose. Finally, the virus particle count and size distribution were determined using a NS300 nanoparticle tracking analyzer (Malvern, Nanosight), and diluted to a final stock concentration of 1×10^{11} particles/ml, UV-inactivated (50 mJ/cm², at a wavelength of 365 nm) and aliquots were frozen at -80 °C. Inactivation was confirmed by

growing of these viruses on Madin-Darby canine kidney (MDCK) cells. A hemagglutininin (HA) assay was performed as described elsewhere[6] to obtain a titer of 2048.

Virus labelling

Influenza viruses were fluorescently labelled using the lipophilic dye octadecyl rhodamine B (R18; Thermo Scientific), which binds the virus membrane with the fluorophore at the aqueous interface. R18 dye was mixed to invactivated virus stocks to a final concentration of 80 nM and incubated in the dark for 2 h on ice. Free dye was subsequently separated from the R18-labelled viruses by adding 25 µl Capto core 700 virus purification beads (GE Healthcare) per 1 ml of virus and incubating by rotating the mixture for 30 min at 4°C. Finally, the beads were cleared from the virus-containing supernatant by pelleting of the beads by centrifugation at 1,200 rpm for 10 min in a table centrifuge at 4°C.

Virus binding studies

Chip fabrication

Flow cells were fabricated according to the procedure described earlier in [7]. A bilayer lift-off recipe was used for fabricating Au electrodes on Mempax glass wafers (Schott). First, LOR 5A (MicroChem) was spin-coated, after which normal lithography was performed on top with Olin OiR 907-17 photoresist (FujiFilm) to create a bilayer resist stack. Electrode patterns were made by exposing the photoresist through a patterned photomask and developing in Olin OPD 4262 (FujiFilm). The develop step washed away the exposed photoresist, and etching through the LOR 5A layer created an undercut. Then, 5 nm Ti and 95 nm Au were deposited via e-beam evaporation (BAK 600, Balzers). The bilayer resist was then removed by sonication in acetone (20 minutes) and isopropanol (10 min) followed by 5 min immersion in OPD 4262, serving as a sacrificial layer to leave patterned Au electrodes on Mempax glass. To fabricate the Cr corrals (10 nm thick) in between the Au electrodes, the same procedure was performed a second time, but in this case following alignment with respect to the Au electrodes.

PDMS flow channel

Silicon flow channel masters were produced by standard photolithography steps and deep reactive ion etching. The polydimethylsiloxane (PDMS) flow channels were prepared from a degassed mixture of 10:1 Sylgard 184 elastomer and curing agent (Dow Corning Corp), which was cast onto the silicon master and cured at 60 °C overnight. The flow channels were cut to size and inlets and outlets were punched using a 1 mm Ø punch (Harris Uni-core, Sigma-Aldrich). After bonding to the chip, a flow channel of 6,000 x 500 x 50 µm was prepared with a second channel entering from the side.

PDMS bonding

Chips were rinsed and sonicated extensively with acetone, ethanol and MilliQ water, and dried prior to UV-ozone exposure (UV/Ozone Procleaner plus, Bioforce Nanosciences) for at least 20 min. After UV exposure, the chips were rinsed with ethanol and water, and dried under a stream of nitrogen. Both cut-out PDMS flow channels and cleaned chips were treated with oxygen plasma for 30 s at 40 W (Plasma prep II, SPI supplies) after which they were bonded immediately. The chips were placed on a hot plate for 10 min at 70 ºC to increase the binding strength. Tygon Microbore tubing S-54-HL (VWR, 0.25 mm inner Ø and 0.75 mm outer Ø) of 80 cm for the inlets and 40 cm for the outlets was inserted into the PDMS. The assembled

μSLB electrophoresis chip was placed in an oven at 60 ºC for 1 h. Leak-free operation was shown for flow rates up to 200 μL/min.

Lipid vesicle preparation

MPPC (1-myristoyl-2-palmitoyl-sn-glycero-3-phosphocholine, Avanti) and DOPC (1,2-dioleoyl-sn-glycero-3-phosphocholine, Avanti) were stored as a 10 mg/ml stock solution in chloroform at -20° C. Biotin-cap-DOPE (1,2-dioleoyl-sn-glycero-3-phosphoethanolamine-N-(cap biotinyl), Avanti) was stored as 0.2 mg/ml solution. Desired molar ratios were mixed in a glass vial, dried under a flow of nitrogen and kept under vacuum for at least 1 h. The resulting film was resuspended by vortexing in MilliQ water at room temperature for DOPC and 50 °C for MPPC to form multilamellar vesicles (MLVs) at 1 mg/ml. The MLV solution was extruded 11 times through a 100 nm polycarbonate membrane (Avanti) at room temperature for DOPC and 50 °C for MPPC. The resulting large unilamellar vesicles (LUVs) were kept at room temperature and used within one week.

SLB formation and functionalization

Before SLB formation, the flow cells were washed with 2% SDS (Sigma-Aldrich), then rinsed with MilliQ, and washed overnight with 2% Hellmanex™ to activate the glass surface. Flow cells were mounted onto a heating plate using Scotch™ tape and rinsed with MilliQ and PBS, while heating to 50 °C. Shortly before LUV incubation, the LUV solution was diluted to 0.5 mg/ml with PBS. The diluted LUV solution was passed through the flow cells through the secondary inlet for 30 min (10 μL/min; primary inlet 1 μL/min PBS) to allow adsorption and rupture of the vesicles on the chips. The chips were then washed with MilliQ (100 μL/min secondary inlet, 10 μL/min primary inlet), after which freshly prepared 0.5 mM hydroxymethylferrocene (FcMeOH, Acros) was passed through the device (50 μL/min, both inlets). A potential difference of 2.0 V was applied over the device for 30 min to induce electrophoresis in the SLBs. Subsequently, the chips were cooled rapidly on a heat exchanger to fix the surface gradient. The flow cells were then rinsed with MilliQ. Bovine serum albumin (Sigma) 50 mg/ml (0.5 ml, 10 μL/min) was passed through the flow cells to form an antifouling layer on the tubing. The flow cells were rinsed with PBS. SA with Alexa Fluor 488 label (Thermo Fischer) 20 μg/ml was passed through the secondary inlet (10 μL/min, primary inlet 1 μL/min). The flow cells were rinsed with PBS. The SA-modified SLBs were inspected with fluorescence microscopy on an Olympus inverted IX71 epi-fluorescence research microscope with X-cite 120PC mercury vapour lamp as light source and a digital Olympus DR70 camera for image acquisition. For Alexa Fluor 488, blue excitation ($460 \leq \lambda_{ex} \leq 490$ nm) and green emission ($505 \leq \lambda_{em} \leq 545$ nm) was filtered using the U-MWG2 Olympus filter cube. Glycans 2,3- and 2,6-$S(LN)_n$-biotin 500 nM solutions were passed through the primary inlet (10 μL/min, secondary inlet 1 μL/min), after which the flow cells were rinsed with PBS. During all steps, care was taken to ensure that no air bubbles entered the flow cell.

Binding studies

Solutions of IAV Puerto Rico/8/1934 mt. Sinai with R18 label were prepared in PBS with 200 μM Zanamivir (GlaxoSmithKline). The virus solution was passed through the primary inlet of the flow cells (1 μL/min, secondary inlet 0.1 μL/min) at a concentration of 10^9 ml^{-1} for $S(LN)_2$ and $S(LN)_3$, and 10^{10} ml^{-1} for $S(LN)_1$. The bound virus was then imaged with fluorescence microscopy. For R18 green excitation ($510 \leq \lambda_{ex} \leq 550$ nm) and red emission ($\lambda_{em} > 590$ nm) was filtered.

Image analysis

8-bit RGB fluorescence micrographs were aligned and cropped into corrals using a custom written MATLAB program that is provided as Supplementary Material. The fluorescence intensities of receptor and virus labels in matching pixels were listed. The receptor density in each pixel was calculated by $\rho_{R,i} = \bar{\rho}_R \cdot \frac{I_i - \bar{I}_{bg}}{\bar{I} - \bar{I}_{bg}}$, with $\bar{\rho}_R$ the average receptor density 2.77 x the biotin% in the SLB, based on a 60 Å^2 lipid footprint,[8,9] I_i the local fluorescence intensity, $\bar{I}$ the average fluorescence intensity and $\bar{I}_{bg}$the average fluorescence intensity of the background. The virus density was normalized between 0 and 1 by finding the maxima of 2D kernel estimations of the data points with the 1,000 lowest and 10% highest receptor densities.

Binding profiles were obtained by fitting Equation 1 with $K_i/N_A V_{explore}$ as fitting parameter, using the built-in *fit* function.

Binding studies with QCM

QCM-D measurements were performed using a QSense analyzer (Biolin Scientific). SiO_2-coated sensors (QSX303, Biolin Scientific) were used. The sensors were cleaned using a 2% (w/v) sodium dodecyl sulfate (SDS) solution and thoroughly rinsed with MilliQ water. Activation was performed with 20 min UV/ozone treatment, and the baseline was made flushing PBS buffer. Measurements were performed at 22 °C and operated with four parallel flow chambers, using two Ismatec peristaltic pumps with a fixed flow rate of 30 µL/min. Throughout this work, the fifth overtone (Δf_5) was used for the normalized frequency and dissipation (ΔD_5). For SLB fabrication, vesicles of DOPC with 2% biotin-cap-DOPE were diluted to a concentration of 0.1 mg/ml in PBS directly before use. SLB formation was achieved by flowing this solution over a cleaned and activated SiO_2 surface. The quality of the SLBs was monitored in situ by QCM-D, where a high quality SLB was characterized by $\Delta f_5 = -24 \pm 1$ Hz and $\Delta D < 0.5 \times 10^{-6}$. In a subsequent step, streptavidin (SA) was bound to the biotin-modified SLB by flushing 0.5µM SA in PBS solution, which was characterized by $\Delta f_5 = -26 \pm 1$. In previous work, we found that biotin-cap-DOPE fractions in the SLB above 2% lead to a densely packed SA layer on top of the SLB[3]. To immobilized the biotinylated $S(LN)_n$ receptors, a solution of each receptor with dummy receptor $(LN)_2$ in varying ratio was passed over the SLB after the stabilization of the frequency with PBS. The final concentration of the glycans was always 1µM leading to a $\Delta f_5 = -2 \pm 1$, depending on the glycans used.

All the titration of PR8 were performed on a biotinylated-SLB functionalized with $S(LN)_n$. PR8 in a concentration range of 8.31 to 166 pM with 100µM Zanamivir in PBS was flushed over the SLBs for 40 min. For each titration step, approximately 90% of the total frequency shift was obtained within the first 30 min. This suggests that the chosen time was sufficient for the viruses to approach thermodynamic equilibrium at these concentrations. Interestingly, at the highest concentration hardly any more virus bound to the surface, indicating that the surface became fully covered.

For a negative control of virus binding on the gel state SLBs that were used in the MAP chip, the QCM-D chamber was heated to 40°C at the start of the experiment. We used vesicles of MPPC with 0.5% biotin-cap-DOPE that were diluted to a concentration of 0.5 mg/ml in PBS directly before use. The chamber was cooled to 22°C before the SA solution was added.

Binding studies with BLI
Discontinuous glycan gradients were obtained by mixing $S(LN)_n$ glycans with the non-sialylated $(LN)_2$ to functionalise SA biosensors (n=8) (Fortebio). Binding studies were performed using a series of 0.83-16.6 pM virus. Plateau values of binding were normalized and plotted as a function of glycan density (range 0 to 3.8 pmol/cm^2, based on the density of SA on biosensors,[10] assuming residual valency 1 for rapidly bound SA[8]). All virus binding experiments were performed *in duplo*.

Code availability
The MATLAB scripts used for analysis of the fluorescence microcopy data of the MAP platform and for fitting the data to the multivalent model are available as Supplementary Material.

Microarray studies
This write-up complies with MIRAGE Glycan Array Guideline v 1.0.

Materials
Virus isolates were produced as described above. Oseltamivir was purchased from Sigma Aldrich [Cat# SML1606].

Arrayer and printing surfaces
Compounds were printed on amine reactive, NHS activated glass slides (NEXTERION ® Slide H) from Schott Inc using a Scienion sciFLEXARRAYER S3 non-contact microarray printer equipped with a Scienion PDC80 nozzle (Scienion Inc). Glycans were dissolved in printing buffer (sodium phosphate, 250 mM, pH 8.5) at a concentration of 100 µM. Each compound was printed in replicates of 6 with a spot volume of ~400 pL, at 20°C and 50% humidity. Slides were blocked with 5 mM ethanolamine in Tris buffer (pH 9, 50 mM) for 1 h at 50 °C and rinsed with DI water after printing.

Glycan Microarray
Quality control was performed using the plant lectins *Erythrina cristagalli agglutinin* (ECA, specific for terminal Gal), *Sambuca nigra agglutinin* (SNA, specific for 2,6-linked Neu5Ac) and *Maackia Amurensis Lectin I* (MAL-I, specific for 2,3-linked Neu5Ac) REF

Sample
Virus was diluted with PBS-T (PBS + 0.1% Tween, 25 µL) and applied to the array surface in the presence of oseltamivir (200 nM) in a humidified chamber for 1 h. It was followed by a succesive rinsing with PBS-T (PBS + 0.1% Tween), PBS and deionized water (2x) and dried by centrifugation and scanned immediately.

Detector and data processing
The stained slides were scanned using an Innopsys Innoscan 710 microarray scanner at the appropriate excitation wavelength. To ensure that all signals were in the linear range of the scanner's detector and to avoid any saturation of the signals various gains and PMT values were employed. Images were analyzed with Mapix software (version 8.1.0 Innopsys) and processed with our home written Excel macro. The average fluorescence intensity and SD was measured for each compound after exclusion of the highest and lowest intensities from the spot replicates (n=4).

Molecular Dynamics

Generation of 3D Molecular Models

The 3D structures of the $S(LN)_n$ glycans were generated using the carbohydrate builder on GLYCAM-Web (www.glycam.org/cb). A linker-biotin moiety was added at the reducing terminus of each glycan using UCSF Chimera.[11]

Initial 3D models of complexes of each glycan bound to tetrameric Streptavidin (SA) were generated by superimposing the biotin moiety onto each of the four biotin residues in a SA-biotin co-crystal structure (PDB ID: 3RY2).

Molecular Dynamics Simulations

All simulations were performed using the Amber18 software suite.[12] Using tleap, the SA-glycan 3D structures were placed in a cubic box of TIP5P[13] water with a 10 water buffer with counterions added to neutralize total charge of the system. The FF14SB,[14] GLYCAM06j,[15] and GAFF[16] force fields were employed for the protein, glycan and spacer-biotin components, respectively. A non-bonded cut-off of 10.0 Å was employed for van der Waals interactions, with electrostatics treated using the particle mesh Ewald model within the PMEMD module.[17] Initial energy minimization (10,000 steps of steepest decent followed by 10,000 steps of conjugate gradient) was performed with a Cartesian restraint (5 kcal mol^{-1}) applied to all solute heavy atoms. The same restraints were applied during a solvent equilibration phase (0.4 ns under nPT conditions at 300 K), followed by a solute equilibration phase (1 ns, nPT, 300 K) during which the Cartesian restraints were retained on protein Cα atoms only. The coordinates from the last step of equilibration were used to start five independent 100 ns production runs for each of the six systems, in which no restraints were employed.

Analysis of the MD simulations

The Ambertools program cpptraj was used to extract 1,000 snapshots from each of the five independent SA-glycan to give a total of 5,000 individual snapshots comprising 20,000 unique shapes for each glycan (four glycans bound per tetrameric SA).

Modeling HA binding to the SA-glycan surface

Models for monomeric binding between a single HA trimer and one SA-glycan were generated by aligning an HA trimer onto the terminus of each of the SA-glycans. This alignment was achieved by superimposing the Gal-residue in the HA-glycan crystal structure (either from PDB ID:1RVX or 3UBE, which are co-crystalized with 2,3-SLN or 2,6-SLN oligosaccharides, respectively) onto the penultimate residue (Gal) in the SA-glycan. Models containing atomic overlaps arising during alignment of the HA-SA moieties were eliminated from further consideration. The percent of shapes (n=5,000 per system) without HA-SA overlaps and the angle between the aligned HA and SA centerlines were calculated using in-house code. This code is available on https://github.com/gitoliver/GlycoProteinBuilder.

Modeling 1 SA - 2 HA binding mode

For each single HA trimer and one SA-glycan model that was generated, the distance between the HA headgroup center and the SA center line was calculated. The ability for each glycan to form the 1SA – 2 HA binding mode was assessed by calculating the distance between the HA headgroup center (average value of each Sia C2 atom) and the SA tetramer center line, then doubling the value. Any values that were less than a HA headgroup diameter (5.6 nm) were discarded.

Modeling 2 SA - 1 HA binding mode

The separate distance between the centers of two SA tetramers bound in two binding sites of a single HA trimer was computed using the MD computed shapes. Each glycan-biotin molecule shape from the MD simulation (n=4,000) was compared against all other shapes placed in a second HA binding site (7.998E+6 combinations). Any shape combination that oriented the SA's such that they would overlap with each other (distance < 5.2 nm) were discarded.

Pulling Simulations to generate bidendate model

The ability for each glycan to form a bidendate binding mode was checked using a previously reported protocol.[3] Glycans with shapes that are theoretically long enough to span two binding sites on a HA (>45Å) were superimposed onto the corresponding HA crystal structure (3UBE for 2,6-SLN, 1RVX for 2,3-SLN) via the Sia-Gal motif. The Sia-Gal motif of the neighboring glycan in the SA tetramer is then brought into the second binding site of the HA by adjusting the intervening glycosidic angles. If the second motif can be brought within ~5 Å, the system is subjected to a pulling MD simulation. NMR distance restraints based on the position of the Sia-Gal in the corresponding crystal structure are gradually introduced over the course of a 100 ns MD simulation to pull the Sia-Gal disaccharide into the binding site. This is followed by a 100 ns simulation during which no restraints are used. Bidendate binding is deemed possible for a glycan if it is able span two binding sites and then remain bound during the unrestrained MD.

Hazards

No unexpected or unusually high safety hazards were encountered.

References

(1) Curk, T.; Bren, U.; Dobnikar, J. Bonding Interactions between Ligand-Decorated Colloidal Particles. *Mol. Phys.* **2018**, *116* (21–22), 3392–3400. https://doi.org/10.1080/00268976.2018.1503354.

(2) Ji, Y.; White, Y. J.; Hadden, J. A.; Grant, O. C.; Woods, R. J. New Insights into Influenza A Specificity: An Evolution of Paradigms. *Curr. Opin. Struct. Biol.* **2017**, *44*, 219–231. https://doi.org/10.1016/j.sbi.2017.06.001.

(3) Peng, W.; de Vries, R. P.; Grant, O. C.; Thompson, A. J.; McBride, R.; Tsogtbaatar, B.; Lee, P. S.; Razi, N.; Wilson, I. A.; Woods, R. J.; Paulson, J. C. Recent H3N2 Viruses Have Evolved Specificity for Extended, Branched Human-Type Receptors, Conferring Potential for Increased Avidity. *Cell Host Microbe* **2017**, *21* (1), 23–34. https://doi.org/10.1016/j.chom.2016.11.004.

(4) Li, T.; Liu, L.; Wei, N.; Yang, J. Y.; Chapla, D. G.; Moremen, K. W.; Boons, G. J. An Automated Platform for the Enzyme-Mediated Assembly of Complex Oligosaccharides. *Nat. Chem.* **2019**, *11* (3), 229–236. https://doi.org/10.1038/s41557-019-0219-8.

(5) Lau, K.; Thon, V.; Yu, H.; Ding, L.; Chen, Y.; Muthana, M. M.; Wong, D.; Huang, R.; Chen, X. Highly Efficient Chemoenzymatic Synthesis of B1–4-Linked Galactosides with Promiscuous Bacterial B1–4-Galactosyltransferases. *Chem. Commun.* **2010**, *46* (33), 6066. https://doi.org/10.1039/c0cc01381a.

(6) Rimmelzwaan, G. F.; Baars, M.; Claas, E. C. J.; Osterhaus, A. D. M. E. Comparison of RNA Hybridization, Hemagglutination Assay, Titration of Infectious Virus and Immunofluorescence as Methods for Monitoring Influenza Virus Replication in Vitro. *J. Virol. Methods* **1998**, *74* (1), 57–66. https://doi.org/10.1016/S0166-0934(98)00071-8.

(7) Overeem, N. J.; Hamming, P. H. (Erik); Huskens, J. Time-Dependent Binding of Molecules and Nanoparticles at Receptor-Modified Supported Lipid Bilayer Gradients in a Microfluidic Device. *ChemistrySelect* **2020**, *5* (31), 9799–9805. https://doi.org/10.1002/slct.202002593.

(8) Dubacheva, G. V.; Araya-Callis, C.; Geert Volbeda, A.; Fairhead, M.; Codée, J.; Howarth, M.; Richter, R. P. Controlling Multivalent Binding through Surface Chemistry: Model Study on Streptavidin. *J. Am. Chem. Soc.* **2017**, *139* (11), 4157–4167. https://doi.org/10.1021/jacs.7b00540.

(9) Nagle, J. F.; Tristram-Nagle, S. Structure of Lipid Bilayers. *Biochim. Biophys. Acta - Rev. Biomembr.* **2000**, *1469* (3), 159–195. https://doi.org/10.1016/S0304-4157(00)00016-2.

(10) Xiong, X.; Coombs, P. J.; Martin, S. R.; Liu, J.; Xiao, H.; McCauley, J. W.; Locher, K.; Walker, P. A.; Collins, P. J.; Kawaoka, Y.; Skehel, J. J.; Gamblin, S. J. Receptor Binding by a Ferret-Transmissible H5 Avian Influenza Virus. *Nature* **2013**, *497* (7449), 392–396. https://doi.org/10.1038/nature12144.

(11) Pettersen, E. F.; Goddard, T. D.; Huang, C. C.; Couch, G. S.; Greenblatt, D. M.; Meng, E. C.; Ferrin, T. E. UCSF Chimera-A Visualization System for Exploratory Research and Analysis. *J. Comput. Chem.* **2004**, *25* (13), 1605–1612. https://doi.org/10.1002/jcc.20084.

(12) Case, D. A.; Ben-Shalom, I. Y.; Brozell, S. R.; Cerutti, D. S.; Cheatham, T. E.; Cruzeiro, V. W. D.; Darden, T. A.; Duke, R. E.; Ghoreishi, D.; Gilson, M. K.; Gohlke, H.; Goetz, A. W.; Greene, D.; Harris, R.; Homeyer, N.; Izadi, S.; Kovalenko, A.; Kurtzman, T.; Lee, T. S.; LeGrand, S.; Li, P.; Lin, C.; Liu, J.; Luchko, T.; Luo, R.; Mermelstein, D. J.; Merz, K. M.; Miao, Y.; Monard, G.; Nguyen, C.; Nguyen, H.; Omelyan, I.; Onufriev, A.; Pan, F.; Qi, R.; Roe, D. R.; Roitberg, A.; Sagui, C.; Schott-Verdugo, S.; Shen, J.; Simmerling, C. L.; Smith, J.; Salomon-Ferrer, R.; Swails, J.; Walker, R. C.; Wang, J.; Wei, H.; Wolf, R. M.; Wu, X.; Xiao, L.; York, D. M.; Kollman, P. A. AMBER 2018, University of California, San Francisco. 2018.

(13) Mahoney, M. W.; Jorgensen, W. L. A Five-Site Model for Liquid Water and the Reproduction of the Density Anomaly by Rigid, Nonpolarizable Potential Functions. *J. Chem. Phys.* **2000**, *112* (20), 8910–8922. https://doi.org/10.1063/1.481505.

(14) Maier, J. A.; Martinez, C.; Kasavajhala, K.; Wickstrom, L.; Hauser, K. E.; Simmerling, C. Ff14SB: Improving the Accuracy of Protein Side Chain and Backbone Parameters from Ff99SB. *J. Chem. Theory Comput.* **2015**, *11* (8), 3696–3713. https://doi.org/10.1021/acs.jctc.5b00255.

(15) Kirschner, K. N.; Yongye, A. B.; Tschampel, S. M.; González-Outeiriño, J.; Daniels, C. R.; Foley, B. L.; Woods, R. J. GLYCAM06: A Generalizable Biomolecular Force Field. Carbohydrates. *J. Comput. Chem.* **2008**, *29* (4), 622–655. https://doi.org/10.1002/jcc.20820.

(16) Wang, J.; Wolf, R. M.; Caldwell, J. W.; Kollman, P. A.; Case, D. A. Development and Testing of a General Amber Force Field. *J. Comput. Chem.* **2004**, *25* (9), 1157–1174. https://doi.org/10.1002/jcc.20035.

(17) Salomon-Ferrer, R.; Götz, A. W.; Poole, D.; Le Grand, S.; Walker, R. C. Routine Microsecond Molecular Dynamics Simulations with AMBER on GPUs. 2. Explicit Solvent Particle Mesh Ewald. *J. Chem. Theory Comput.* **2013**, *9* (9), 3878–3888. https://doi.org/10.1021/ct400314y.